ON THE DESIGN OF OPTIMAL COMPLIANT WALLS FOR TURBULENCE CONTROL

M. Luhar
Aerospace and Mechanical Engineering
University of Southern California
Los Angeles, CA 90089, USA
luhar@usc.edu

A.S. Sharma
Engineering and the Environment
University of Southampton
Highfield, Southampton, SO17 1BJ, UK
a.sharma@soton.ac.uk

B.J. McKeon
Graduate Aerospace Laboratories
California Institute of Technology
Pasadena, CA 91125, USA
mckeon@caltech.edu

ABSTRACT

This paper employs the theoretical framework developed by Luhar *et al.* (2015, *J. Fluid Mech.*, **768**, 415-441) to consider the design of compliant walls for turbulent skin friction reduction. Specifically, the effects of simple spring-damper walls are contrasted with the effects of more complex walls incorporating tension, stiffness and anisotropy. Despite the differing physical responses, all the walls tested exhibit two important common features. First, the effect of the walls (positive or negative) is greatest at conditions close to resonance, with sharp transitions in performance across the resonant frequency or phase speed. In general, turbulent flow structures with frequencies (or phase speeds) below resonance are further amplified, while higher-frequency structures are suppressed. Compliant walls are also predicted to have a more pronounced effect on the slower-moving low frequency structures because such structures generally have larger wall-pressure signatures. Second, two-dimensional (spanwise constant) structures are particularly susceptible to further amplification. This is consistent with previous experiments and simulations, suggesting that mitigating the rise of such two-dimensional structures is essential to designing performance-improving walls. The above observations are used to develop specific design guidelines for compliant walls.

INTRODUCTION

The design of compliant surfaces for turbulent skin friction reduction has attracted significant attention since the early experiments of Kramer (1961). However, despite many experimental (e.g. Bushnell *et al.*, 1977; Gad-el-Hak *et al.*, 1984; Lee *et al.*, 1993; Choi *et al.*, 1997) and numerical (e.g. Endo & Himeno, 2002; Xu *et al.*, 2003; Kim & Choi, 2014) efforts, there are few definitive results. Broadly, the direct numerical simulations (DNS) and experiments both show that *softer* surfaces often give rise to energetic two-dimensional (i.e. spanwise constant) wave-like motions, which can cause a substantial increase in skin friction. *Harder* surfaces appear to have little impact on

the flow, although some qualitative flow visualization experiments hint at an intermittent relaminarization-like phenomenon (Lee *et al.*, 1993).

One of the major challenges associated with developing performance-enhancing surfaces is the extent of the parameter space to be explored. Even the simplest spring-damper walls considered in DNS depend on three independent parameters: a mass ratio, a spring constant and a damping coefficient. The viscoelastic layers tested frequently in experiments (Gad-el-Hak *et al.*, 1984; Lee *et al.*, 1993) depend on at least five different parameters: two elastic constants which determine the shear- and longitudinal wave speeds, the mass density, a viscous relaxation time, and the layer thickness. Clearly, independent evaluation and optimization of these parameters in DNS or experiment is impractical, indicating the need for a computationally inexpensive theoretical framework to study turbulence-compliant wall interactions.

In an effort to address this need, Luhar *et al.* (2015) recently extended the resolvent formulation proposed by McKeon & Sharma (2010). Under this formulation, the turbulent velocity field is expressed as a superposition of propagating modes, identified via a gain-based decomposition of the Navier-Stokes equations (NSE). Compliant surfaces are introduced via changes in the kinematic and dynamic boundary conditions. In particular, a complex wall admittance is used to define the relationship between the pressure and wall-normal velocity at the wall. This change in the boundary conditions leads to a change in the gain and structure of the modes, whereby a reduction in gain is interpreted as mode suppression.

Luhar *et al.* (2015) show that this approach predicts the amplification of the quasi two-dimensional structures observed recently in DNS (Kim & Choi, 2014) with minimal computation. Further, the formulation also enables an optimization of surface properties (i.e. wall admittance) to suppress flow structures known to be energetic in wall turbulence. This blind optimization suggests that negative-damping walls are required to suppress the near-wall (NW) cycle, identified by various researchers as essential to con-

1

trolling wall turbulence (e.g. Bushnell *et al.*, 1977). However, walls with positive damping could be effective against the so-called superstructures or very-large-scale motions (VLSMs) that appear at high Reynolds number. Unfortunately, Luhar *et al.* (2015) show that the optimal walls identified via this procedure also have negative effects elsewhere in spectral space, with slow-moving spanwise-constant structures particularly susceptible to further amplification.

The purpose of the present paper is to build on the above findings and evaluate the effect of varying wall models in greater detail, looking closely at the sensitivity to two-dimensional structures. While Luhar *et al.* (2015) focused primarily on a spring-damper wall, this paper introduces the effects of tension, stiffness and anisotropy. Further, we also consider the effects of varying mass ratios to contrast aerodynamic and hydrodynamic applications.

THEORY
Resolvent Formulation

The resolvent formulation considers the turbulent velocity field, $\mathbf{u}$, to be a superposition of highly amplified velocity structures, or modes, identified via a gain-based decomposition of the Fourier-transformed Navier-Stokes equations (NSE). For each wavenumber-frequency combination $\mathbf{k} = (\kappa_x, \kappa_z, c = \omega/\kappa_x)$, where κ_x and κ_z are the streamwise and spanwise wavenumbers, ω is the frequency and c is the phase speed, the NSE are interpreted as a forcing-response system[1]:

$$\begin{bmatrix} \mathbf{u_k} \\ p_\mathbf{k} \end{bmatrix} = \left(-i\omega \begin{bmatrix} \mathbf{I} & \\ & 0 \end{bmatrix} - \begin{bmatrix} \mathscr{L}_\mathbf{k} & -\nabla_\mathbf{k} \\ \nabla_\mathbf{k}^T & 0 \end{bmatrix} \right)^{-1} \begin{bmatrix} \mathbf{I} \\ 0 \end{bmatrix} \mathbf{f_k} = \mathscr{H}_\mathbf{k} \mathbf{f_k} \tag{1}$$

The nonlinear terms are interpreted as the forcing to the system, $(\mathbf{u} \cdot \nabla \mathbf{u})_\mathbf{k} = \mathbf{f_k}(y) \exp i(\kappa_x x + \kappa_z z - \omega t)$, and the resolvent operator, $\mathscr{H}_\mathbf{k}$, maps this forcing to the velocity and pressure responses, e.g. $\hat{\mathbf{u}}_\mathbf{k} = \mathbf{u_k}(y) \exp i(\kappa_x x + \kappa_z z - \omega t)$. Here, x, y and z are the streamwise, wall-normal and spanwise coordinates, respectively, and t is time. A subscript $\mathbf{k}$ denotes an individual Fourier component. In Eq. 1, $\nabla_\mathbf{k}$ and $\nabla_\mathbf{k}^T$ represent the Fourier-transformed gradient and divergence operators, and $\mathscr{L}_\mathbf{k}$ is the linearized Navier-Stokes operator.

A singular value decomposition (SVD) of the discretized resolvent operator $\mathscr{H}_\mathbf{k} = \sum_m \psi_m(y) \sigma_m \phi_m^*(y)$ yields a set of orthonormal forcing (ϕ_m) and response (ψ_m) modes, ordered based on the input-output gain ($\sigma_1 > \sigma_2 > \sigma_m > ...$). Forcing in the direction of the mth forcing mode with unit amplitude results in a response in the direction of the mth response mode amplified by factor σ_m. Thus, forcing $\mathbf{f_k}(y) = \phi_1(y)$ creates a response $[\mathbf{u_k}(y), p_\mathbf{k}(y)]^T = \sigma_1 \psi_1(y)$. Note that the resolvent operator is scaled prior to performing the SVD to enforce an L^2 norm for the velocity, $\mathbf{u_k}$, and forcing, $\mathbf{f_k}$ (see Luhar *et al.*, 2015).

In general, for $\mathbf{k}$ combinations energetic in natural turbulence, the resolvent operator tends to be low rank. A limited number of input directions are highly amplified, often with $\sigma_1 \gg \sigma_2$, and so the velocity and pressure fields can be reasonably approximated by the first response mode

---

[1] This paper focuses on turbulent channel flows but the approach can be generalized to pipe and boundary layer flows as well.

$[\mathbf{u_k}(y), p_\mathbf{k}(y)]^T \sim \psi_1(y)$. Recent studies show that this rank-1 approximation captures many of the key features of wall-bounded turbulent flows, including the emergence of coherent structures and their footprint in the wall pressure field (Sharma & McKeon, 2013; Luhar *et al.*, 2014a). Further, the rank-1 modes also form useful building blocks for low-order models of flow control (Luhar *et al.*, 2014b). As a result, the rest of this paper only considers the first singular values and modes, dropping the subscript 1 for convenience.

Boundary Conditions

The effect of the compliant wall is introduced by changing the boundary conditions on velocity and pressure within the resolvent (Eq. 1) before computing the SVD. Assuming small wall deformation $\eta_\mathbf{k}$, the linearized kinematic boundary conditions on streamwise ($u_\mathbf{k}$) and wall-normal ($v_\mathbf{k}$) velocities at the bottom wall ($y = 0$) become:

$$v_\mathbf{k}(0) = -i\omega\eta_\mathbf{k}; \; u_\mathbf{k}(0) = -\eta_\mathbf{k} \frac{\partial U}{\partial y}\Big|_{y=0} \tag{2}$$

where U is the mean velocity profile. The dynamic boundary condition is expressed as a wall admittance, Y, linking wall-normal velocity and pressure:

$$v_\mathbf{k}(0) = Y p_\mathbf{k}(0) \tag{3}$$

Similar boundary conditions apply at the top wall, $y = 2$ (y is normalized by the channel half-height, h). Though, for identical walls, the sign of the admittance changes due to the differing symmetries of the wall-normal velocity and pressure fields across the centerline. Note that the linearized boundary conditions and the requirement of a mean velocity profile are some of the key limitations of the present approach. These limitations are discussed in greater detail by Luhar *et al.* (2015).

The admittance Y dictates the relative phase and amplitude of the wall-normal velocity and the pressure at the wall. As such, it can be used to represent walls of known material properties. For example, the most commonly used model for compliant walls involves a tensioned plate supported on a bed of springs and dampers. For such walls, the admittance can be expressed as (Xu *et al.*, 2003):

$$Y = \frac{i\omega}{-C_m\omega^2 - i\omega C_d + C_{ke}} \tag{4}$$

where C_m and C_d are the dimensionless mass ratio and damping coefficient, and

$$C_{ke} = C_k + C_t(\kappa_x^2 + \kappa_z^2) + C_s(\kappa_x^4 + 2\kappa_x^2\kappa_z^2 + \kappa_z^4) \tag{5}$$

is a wavenumber-dependent effective spring constant. The parameters C_k, C_t and C_s represent the dimensionless spring constant, tension and flexural rigidity. All of the above parameters are normalized based on the channel half-height h, friction velocity u_τ and fluid density ρ.

Table 1. Different walls optimized to suppress resolvent modes resembling VLSMs. The damping coefficient is $C_d = 0.4688$ in all cases.

Case	C_m	C_k	C_s	C_t
base	2	510.4	0	0
high C_m	20	5118	0	0
tension	2	0	0	5.053
stiffness	2	0	0.0500	0
anisotr.	2	0	0	$C_{tx} = 288$
				$C_{tz} = 2.224$

Optimal Walls

In addition to evaluating the effects of the wall parameters individually, the resolvent framework can also be used to solve the inverse problem: finding an optimal Y that leads to the most favorable effect on the turbulent flow structures of interest. Luhar *et al.* (2015) pursued this optimization for modes resembling the NW-cycle and VLSMs at friction Reynolds number $Re_\tau = u_\tau h / \nu = 2000$ (ν is the kinematic viscosity). The NW-cycle was represented by the wavenumber-frequency combination $\mathbf{k} = (\kappa_x, \kappa_z, c^+) = (12, 120, 10)$ and the VLSMs were represented by $\mathbf{k} = (1, 10, 16)$. These wavenumbers translate into structures of streamwise and spanwise wavelength $(\lambda_x^+, \lambda_z^+) \approx (1050, 105)$ and $(\lambda_x^+, \lambda_z^+) \approx (12500, 1250)$, respectively. Optimality was defined in two different ways: walls that lead to the greatest mode suppression (i.e. lowest $\sigma_\mathbf{k}$) or the largest reduction in the channel-integrated Reynolds stress contribution from the mode (per Fukagata *et al.*, 2002). Note that a superscript $+$ denotes normalization with respect to u_τ and ν.

For brevity, this paper focuses on the optimal gain-reducing wall for modes resembling the VLSMs. A simple pattern search procedure shows that a wall with admittance $Y = -2.0385 - 0.4387i$ leads to the greatest reduction in singular value for such modes, with the ratio of compliant to rigid-wall (null-case) singular values being $\sigma_{\mathbf{k}c}/\sigma_{\mathbf{k}0} = 0.52$. Note that this optimization is blind to the physical properties of the compliant walls. For walls characterized by Eq.4-5, this optimal admittance can be realized through any combination of springs, tension and stiffness. To evaluate how these factors affect performance, particularly with respect to the excitation of spanwise-constant modes, we test the different walls listed in Table 1, each of which has admittance $Y = -2.0385 - 0.4387i$ for $\mathbf{k} = (1, 10, 16)$.

The base case is the wall evaluated by Luhar *et al.* (2015), which represents a simple spring-damper system such that $C_{ke} = C_k$ and $C_m = 2$. The high $C_m (= 20)$ case is similar but requires a larger spring constant to counteract the increase in mass ratio. The next two cases in Table 1 remove the spring support but introduce the effects of tension and stiffness, such that $C_{ke} = C_t(\kappa_x^2 + \kappa_z^2)$ and $C_{ke} = C_s(\kappa_x^4 + 2\kappa_x^2\kappa_z^2 + \kappa_z^4)$, respectively. The last case introduces the effects of anisotropy through differing streamwise and spanwise tension. Despite the physical differences, all of the walls are resonant just below the mode frequency $\omega = 16$ for $\kappa_x = 1$ and $\kappa_z = 10$. Specifically, the resonant frequency is $\omega_r = \omega_n \sqrt{1 - 2\zeta^2} = 15.97$, where $\omega_n = \sqrt{C_{ke}/C_m}$ is the undamped natural frequency of the wall and $\zeta = C_d/(2\sqrt{C_{ke}C_m})$ is the damping factor.

RESULTS
Effect of Mass Ratio

One of the key differences between aerodynamic and hydrodynamic flows over compliant walls is the mass ratio, which is determined by the ratio of the solid density to the fluid density. While $C_m \sim O(1)$ is appropriate for hydrodynamic applications, it is expected that $C_m \sim O(10^3)$ for aerodynamic applications. A high mass ratio translates into a much smaller wall response to fluid pressure perturbations away from resonance, which in turn means that the wall does not significantly influence the flow structures. This is illustrated by the base case and high C_m results shown in Fig. 1. The spectral region over which the compliant wall has a strong influence on the singular values (positive or negative) shrinks significantly as the mass ratio is increased from $C_m = 2$ (Fig. 1a) to $C_m = 20$ (Fig. 1b). As an example, for $\kappa_x = 10$ the base case wall affects modes with speeds up to $c^+ \approx 8$, while the $C_m = 20$ wall only affects modes with speeds up to $c^+ \approx 3$. Note that the region of influence in both cases is centered approximately around the resonant frequency, where the magnitude of the admittance $|Y|$ peaks. In general, the compliant wall seems to have a positive influence (suppression) on modes with frequencies higher than the resonant frequency (i.e. above the solid black line) and a negative effect on modes with lower frequencies.

Also shown in Fig. 1 are isocontours of the magnitude of the wall admittance $|Y|$ (dashed lines) at level 0.01. A comparison of Fig. 1a and Fig. 1b shows that the region enclosed by these isocontours reduces rapidly with increasing mass ratio. More quantitatively, the half-power bandwidth of a spring-damper system is expected to scale as $\zeta \omega_n \sim C_m^{-1}$ for $\zeta \ll 1$. So the ten-fold increase in the mass-ratio translates into a roughly ten-fold decrease in the frequency bandwidth of the wall. This bandwidth would decrease even further for $C_m \sim O(10^3)$, suggesting that compliant walls are unlikely to be practical for aerodynamic applications without the development of novel lightweight materials.

Note that the decrease in the spectral influence of the compliant wall is roughly consistent with the decrease in the wall bandwidth. However, there are regions where the wall influences the flow despite low $|Y|$ (e.g. for very slow modes with $c^+ < 1$) and where the wall does not have an appreciable effect even at resonance (e.g. for faster modes with $c^+ > 17$). This is because the influence of the wall is determined both by the admittance as well as the magnitude of the wall-pressure fluctuations. In general, the magnitude of the wall pressure fields associated with the modes decreases with increasing mode speed c^+ (i.e. as the modes move further away from the wall, see Luhar *et al.*, 2014a), and so slower modes are likely to interact with compliant walls to a larger extent.

Comparing Springs, Tension and Stiffness

Next we compare the effects of a compliant wall on a spring support with a tensioned membrane and a stiff plate. For the simple spring-damper system, the fluid-structure interactions are dependent solely on frequency. Moreover, the wall does not communicate in the streamwise and spanwise directions, which means that it cannot support wave propagation. In contrast, tensioned membranes and stiff plates have a wavenumber-dependent effective spring constant (Eq. 5) and can support wave propagation. This means that the three different walls have varying effects
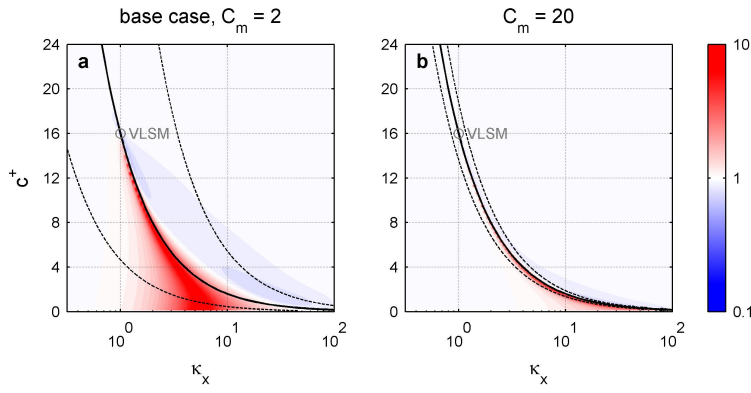
Figure 1. Shaded contours showing the ratio of compliant wall to null-case singular values, $\sigma_{\mathbf{k}c}/\sigma_{\mathbf{k}0}$, for the base case (a) and high C_m (b) walls listed in Table 1. Blue regions denote mode suppression while red regions indicate further amplification. The solid black lines indicate the resonant frequency. The dashed lines represent isocontours of the magnitude of the admittance $|Y|$ at level 0.01. All results correspond to $\kappa_z = 10$.
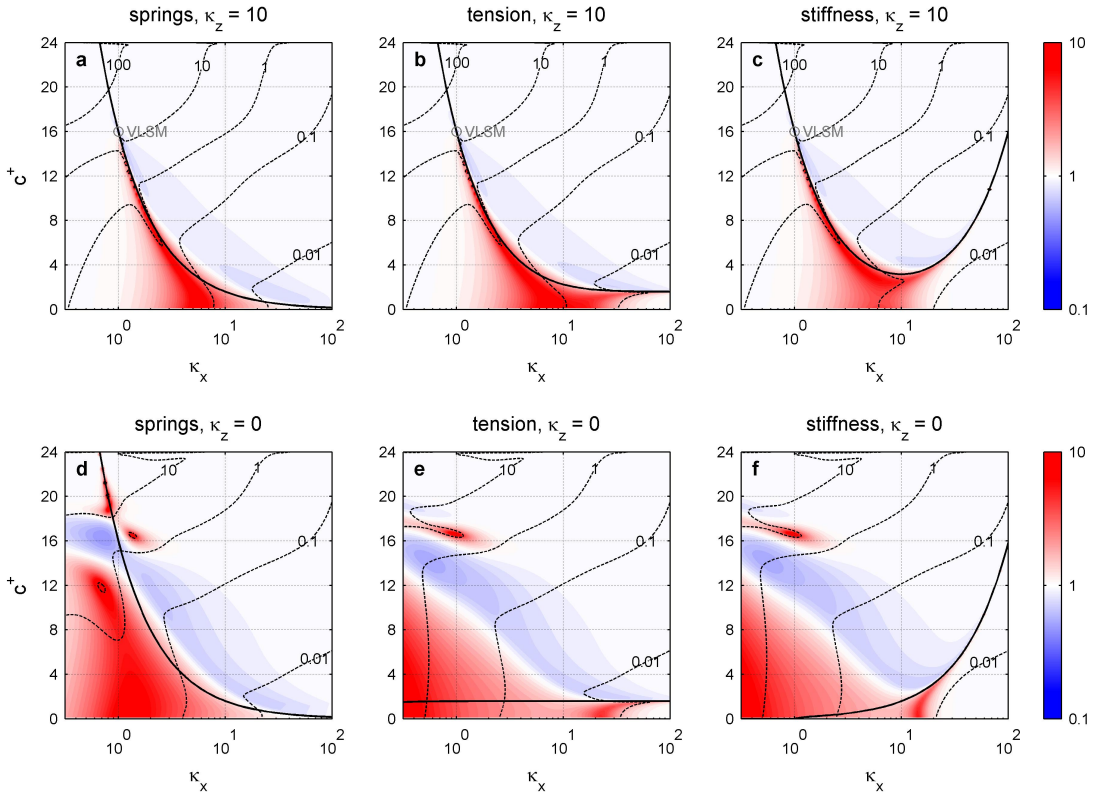

Figure 2. Shaded contours showing the singular value ratio $\sigma_{\mathbf{k}c}/\sigma_{\mathbf{k}0}$ as a function of streamwise wavenumber and mode speed. Blue regions denote mode suppression and red regions denote amplification. Plots (a,d), (b,e) and (d,f) represent the base case, tensioned wall and stiff wall listed in Table 1, respectively. The dashed contours indicate the magnitude of the singular values $\sigma_{\mathbf{k}c}$ over the compliant walls. The solid lines show the resonant frequency.

across spectral space, despite being optimized to suppress the VLSM-type modes.

The above effects are best understood in terms of the resonant frequency ω_r. Like the results shown in the previous section, for $\kappa_z = 10$, modes with frequencies below the resonant frequency are further amplified by the compliant walls while modes with higher frequencies are generally suppressed (Fig. 2a-c). However, the resonant frequency

(solid black lines) varies substantially across the three different cases. For the basic spring-damper wall, the resonant frequency is constant, and so the effect of the wall is centered around modes with $c^+\kappa_x = \omega_r$, or $c^+ \sim \kappa_x^{-1}$ (Fig. 2a). For the tensioned membrane and stiff plate, the response is centered around a similarly decreasing function $c^+ = f(\kappa_x)$ for $\kappa_x \ll \kappa_z(= 10)$ (Fig. 2b,c). This is because the effective spring constant is dominated by the spanwise

4

wavenumber dependence for $\kappa_x \ll \kappa_z$, leading to essentially constant $C_{ke} \approx C_t \kappa_z^2 \approx 505$ and $C_{ke} \approx C_s \kappa_z^4 \approx 500$ for the results shown in Fig. 2b,c. However, as $\kappa_x \gg \kappa_z$, the effective spring constant for the walls is dominated by the streamwise dependences $C_{ke} \approx C_t \kappa_x^2$ and $C_{ke} \approx C_s \kappa_x^4$, which translates into resonant frequencies $\omega_r \approx \kappa_x \sqrt{C_t/C_m}$ and $\omega_r \approx \kappa_x^2 \sqrt{C_s/C_m}$. This means that the maximum admittance is found at near-constant $c^+ \approx \sqrt{C_t/C_m} = 1.59$ for the tensioned membrane (Fig. 2b) and is an increasing function $c^+ = f(\kappa_x)$ for the stiff plate (Fig. 2c).

Figures 2d-f show that all three walls also lead to significant amplification of two-dimensional ($\kappa_z = 0$) structures, which is consistent with previous experiments and DNS. All three cases exhibit a repeating amplification-suppression-amplification pattern with increasing mode speed, at least for $\kappa_x < 5$. For example, at $\kappa_x = 1$, modes with $c^+ < 10$ are further amplified, modes with $c^+ \approx 10$ to $c^+ \approx 16$ are suppressed and modes with $c^+ > 16$ are again further amplified. The speeds at which these transitions occur generally decrease with increasing κ_x, although wall resonance plays a role as well (Fig. 2d, solid black line). In general, there appear to be two classes of mode that are further amplified over compliant walls. Long, slow-moving modes with $\kappa_x < 5$ and $c^+ < 7$ are amplified regardless of the wall properties, at least for the walls tested. The second class of modes that is further amplified is linked to wall resonance and is generally of smaller wavelength (see e.g. $\kappa_x \approx 10$ in Fig. 2e,f).

Note once again that the resonant frequency, and hence wave speed, varies significantly across the three different cases. The wave speed corresponding to resonance is a decreasing function of κ_x for the spring-damper wall (Fig. 2d), constant for the tensioned membrane (Fig. 2e, $c^+ \approx \sqrt{C_t/C_m}$, i.e. the free-wave speed of the wall), and an increasing function of κ_x for the stiff plate (Fig. 2f).

Anisotropy and Wall-based Instability

Finally, we introduce the effects of anisotropy by testing the effects of a wall with different streamwise and spanwise tension coefficients $C_{tx} = 288$ and $C_{tz} = 2.224$, so that $C_{ke} = C_{tx} \kappa_x^2 + C_{tz} \kappa_z^2$ (Eq. 5). This anisotropy changes the resonant frequency of the wall (Fig. 3a,b) and the free wave speed is now $c^+ \approx \sqrt{C_{tx}/C_m} = 12$. However, the trends observed in the previous section remain. In particular, there is a sharp transition in performance across the resonant frequency for the $\kappa_z = 10$ modes, and spanwise-constant ($\kappa_z = 0$) modes are susceptible to significant further amplification. There are two classes of highly-amplified spanwise-constant modes: long, slow-moving structures and shorter (e.g. $\kappa_x = 1, c^+ = 1$, marked c in Fig. 3b), faster structures moving at close to the free wave speed (e.g. $\kappa_x \approx 4, c^+ = 11$, marked d in Fig. 3b).

The above predictions are broadly consistent with the observations of Gad-el-Hak *et al.* (1984); Gad-el-Hak (1986), who showed that elastic and viscoelastic layers under turbulent boundary layers gave rise to two distinct classes of surfaces waves: the first, termed static divergence, were very long, slow-moving (nearly static) structures, while the second class of surface waves had shorter wavelengths and faster phase speeds, comparable to the free shear wave speed of the layer. The experiments suggest that the static-divergence waves appear preferentially for viscoelastic coatings while the faster waves appear preferentially for elastic layers. This effect of the viscosity (i.e. the damping in our model) remains to be explored.

Figures 3c,d show the structure associated with the two highly-amplified modes identified in Fig. 3b. Although the modes have vastly different wavelengths and speeds, the overall structure is similar. Specifically, the streamwise velocities associated with the modes are confined to a very small layer close to the wall, above which the velocities are primarily in the up-down wall-normal direction. Further, the magnitude of the wall-pressure field is largest over surface troughs and smallest over surface peaks, i.e. high pressures coincide with downward deflections and vice versa, as expected physically.

CONCLUSION

The results presented in this paper suggest two important guidelines for the design of compliant surfaces to reduce turbulent skin friction.

First, the sharp transitions in performance across the resonant frequency of the wall suggest that compliant walls must be slightly detuned and resonant at frequencies *below* the spectral region of interest. Although Luhar *et al.* (2015) employed single wavenumber-frequency combinations as models for VLSMs and the NW-cycle, in reality these structures occupy a region in spectral space. As such, designing a compliant wall with sharp transition in performance within this region is unlikely to be effective. Note that this transition in performance may be linked to the change in the pressure-wall deflection phase relationship across the natural frequency, i.e. as the imaginary component of Y changes sign.

Second, the susceptibility to spanwise-constant structures must be minimized. This is likely to be difficult given that most natural materials tend to serve as low-pass filters. That is, the effect spring constant generally decreases with decreasing κ_z. One potential solution is to employ walls that are in spanwise compression, $C_{tz} < 0$, which would lead to a larger effective spring constant for $\kappa_z = 0$. Other possibilities include periodic spanwise breaks in the compliant material to disperse the spanwise-constant structures, or the use of mechanical metamaterials which ensure that the curvatures in the streamwise and spanwise directions are coupled, i.e. such that surface waves with $\kappa_z = 0$ and $\kappa_x \neq 0$ cannot be generated.

REFERENCES

Bushnell, D. M., Hefner, J. N. & Ash, R. L. 1977 Effect of compliant wall motion on turbulent boundary layers. *Physics of Fluids* **20**, S31–S48.

Choi, K. S., Yang, X., Clayton, B. R., Glover, E. J., Atlar, M., Semenov, B. N. & Kulik, V. M. 1997 Turbulent drag reduction using compliant surfaces. *Proceedings of the Royal Society A-Mathematical Physical and Engineering Sciences* **453** (1965), 2229–2240.

Endo, T. & Himeno, R. 2002 Direct numerical simulation of turbulent flow over a compliant surface. *Journal of Turbulence* **3**, 1–10.
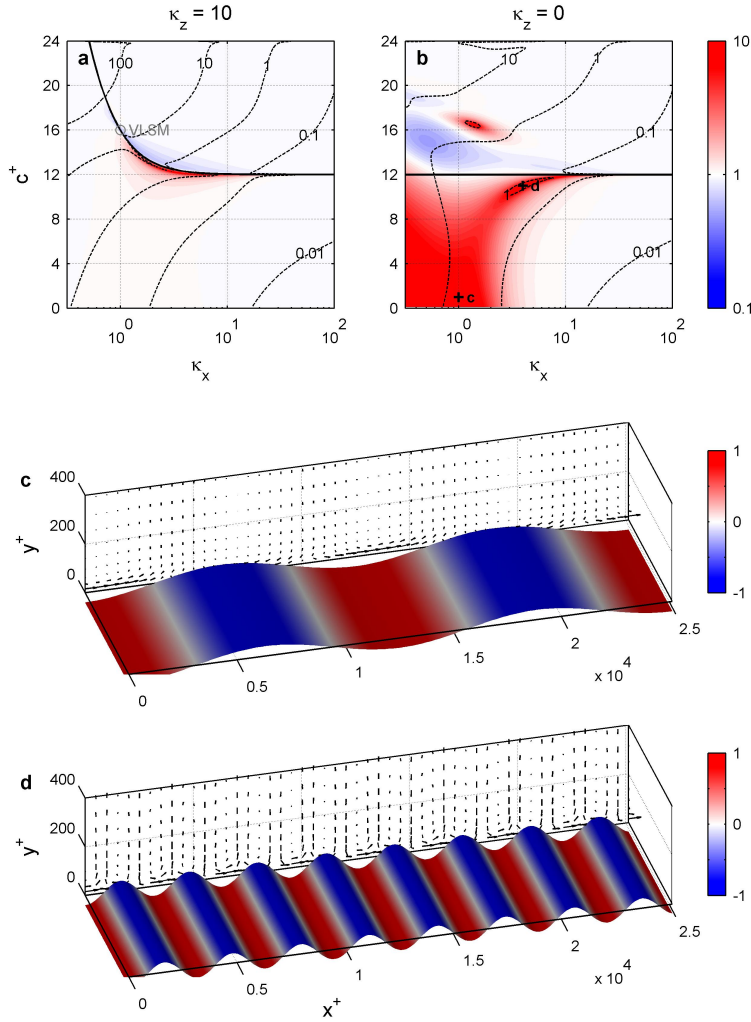
Figure 3. Shaded contours showing the singular value ratio $\sigma_{\mathbf{k}c}/\sigma_{\mathbf{k}0}$ for $\kappa_z = 10$ (a) and $\kappa_z = 0$ (b) over the anisotropic wall listed in Table 1. Blue regions denote mode suppression and red regions denote amplification. Plots (c) and (d) show the structure of the highly amplified two-dimensional modes marked in (b), representing wave number frequency combinations $\mathbf{k} = (\kappa_x, \kappa_z, c^+) = (1, 0, 1)$ and $\mathbf{k} = (3.8, 0, 11)$, respectively. The shading on the compliant wall indicates the normalized pressure field. The vectors show the streamwise and wall-normal velocity fields. Wall deflection not to scale.

Fukagata, K., Iwamoto, K. & Kasagi, N. 2002 Contribution of Reynolds stress distribution to the skin friction in wall-bounded flows. *Physics of Fluids* **14** (11), 73–76.

Gad-el-Hak, M. 1986 The response of elastic and viscoelastic surfaces to a turbulent boundary layer. *Journal of Applied Mechanics* **53** (1), 206–212.

Gad-el-Hak, M., Blackwelder, R. F. & Riley, J. J. 1984 On the interaction of compliant coatings with boundary-layer flows. *Journal of Fluid Mechanics* **140**, 257–280.

Kim, E. & Choi, H. 2014 Space-time characteristics of a compliant wall in a turbulent channel flow. *Journal of Fluid Mechanics* **756**, 30–53.

Kramer, M. O. 1961 The dolphin's secret. *Journal of the American Society for Naval Engineers* **73**, 103–108.

Lee, T., Fisher, M. & Schwarz, W. H. 1993 Investigation of the stable interaction of a passive compliant surface with a turbulent boundary layer. *Journal of Fluid Mechanics* **257**, 373–401.

Luhar, M., Sharma, A. S. & McKeon, B. J. 2014a On the structure and origin of pressure fluctuations in wall turbulence: predictions based on the resolvent analysis. *Journal of Fluid Mechanics* **751**, 38–70.

Luhar, M., Sharma, A. S. & McKeon, B. J. 2014b Opposition control within the resolvent analysis framework. *Journal of Fluid Mechanics* **749**, 597–626.

Luhar, M., Sharma, A. S. & McKeon, B. J. 2015 A framework for studying the effect of compliant surfaces on wall turbulence. *Journal of Fluid Mechanics* **768**, 415–441.

McKeon, B. J. & Sharma, A. S. 2010 A critical-layer framework for turbulent pipe flow. *Journal of Fluid Mechanics* **658**, 336–382.

Sharma, A. S. & McKeon, B. J. 2013 On coherent structure in wall turbulence. *Journal of Fluid Mechanics* **728**, 196–238.

Xu, S., Rempfer, D. & Lumley, J. 2003 Turbulence over a compliant surface: numerical simulation and analysis. *Journal of Fluid Mechanics* **478**, 11–34.